APL Photonics

RESEARCH ARTICLE | JUNE 04 2025

Wide angle tolerant solar spectral splitter for lateral tandem solar cells

M. L. Schubert ; J. D. Fischbach ; M. Nyman ; L. Lüer ; C. J. Brabec ; C. Rockstuhl ;
T. J. Sturges

APL Photonics 10, 066105 (2025)
https://doi.org/10.1063/5.0266467

Articles You May Be Interested In

Broadband and fabrication tolerant polarization splitter–rotator on thin-film lithium niobate

APL Photonics (January 2025)

Silicon nitride waveguide polarization rotator and polarization beam splitter for chip-scale atomic systems

APL Photonics (April 2022)

Improving Savonius turbine efficiency with splitter and barrier cylinder deflector design: A Taguchi method study

Physics of Fluids (November 2023)

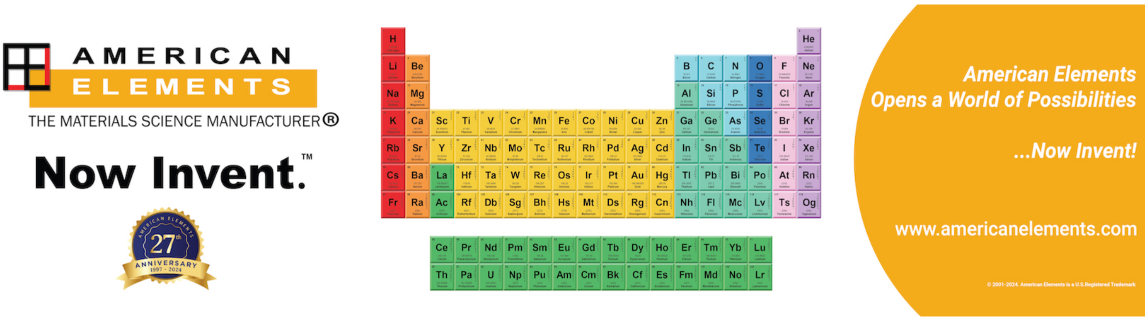

AIP Publishing

APL Photonics ARTICLE pubs.aip.org/aip/app

Wide angle tolerant solar spectral splitter for lateral tandem solar cells

Cite as: APL Photon. 10, 066105 (2025); doi: 10.1063/5.0266467
Submitted: 19 February 2025 • Accepted: 16 May 2025 •
Published Online: 4 June 2025

M. L. Schubert,[1,a)] **J. D. Fischbach,**[1] **M. Nyman,**[1] **L. Lüer,**[2] **C. J. Brabec,**[2,3] **C. Rockstuhl,**[1,4] **and T. J. Sturges**[4,b)]

AFFILIATIONS

[1] Karlsruhe Institute of Technology (KIT), Institute of Nanotechnology, Karlsruhe, Germany
[2] Friedrich-Alexander-Universität Erlangen-Nürnberg (FAU), Institute of Materials for Electronics and Energy Technology (i-MEET), Erlangen, Germany
[3] Helmholtz Institute Erlangen-Nürnberg (HI ERN), Erlangen, Germany
[4] Karlsruhe Institute of Technology (KIT), Institute of Theoretical Solid State Physics, Karlsruhe, Germany

[a)] **Author to whom correspondence should be addressed:** marie.schubert@kit.edu
[b)] **Electronic mail:** thomas.sturges@kit.edu

ABSTRACT

Maximizing the power conversion efficiency of solar cells plays a crucial role in upscaling solar energy production. Combining two or more solar cells with different bandgaps into a multi-junction tandem solar cell lowers thermalization losses and increases the power conversion efficiency. While the best efficiencies have been achieved by vertically stacking solar cells, the fabrication process is technologically demanding and leads to high production costs. Novel photovoltaic materials such as organic photovoltaics allow solution processing, which could enable cost effective production of lateral multijunctions, where the single subcells are aligned side by side. To fully unlock their optimal performance, lateral tandems require careful light management, redirecting different spectral bands to the corresponding solar cell. So far, solar spectral splitters suffered from a strong angle dependency, which caused degradation in performance at the slightest deviation from normal incidence. In this contribution, we reduce this limitation and achieve an enhancement in the conversion efficiency across a wide range of incident angles by inverse designing a solar spectral splitter composed of two free-form microstructured surfaces on the top and bottom of a supporting glass substrate. Moreover, thanks to the versatility of our methodology, we can tailor the angle-dependent functionality of our device. As such, we also design devices that are optimized to provide enhanced performance at certain oblique angles, which correspond to different times of the day, e.g., when the unit price of energy is higher.

I. INTRODUCTION

Single-junction silicon solar cells are the current standard for solar energy production. However, their power conversion efficiency is limited to 29.4% by Auger recombination.[1] In addition, any single-junction device is limited in power conversion efficiency to around 33% by the detailed-balance limit for solar cells.[2] This limit can be overcome by combining solar cells with different bandgaps into a multi-junction tandem solar cell. By using multiple subcells that are optimized for different portions of the total spectrum, these solar cells can absorb light across a broader range of wavelengths and with reduced thermalization losses.[3] This multi-junction technique has provided the world record efficiency of 47.6% for vertically stacked tandem solar cells under a light concentration of 665 suns.[4] However, this type of tandem solar cell has the main disadvantage of being expensive and complicated to produce.[3] The upper layer structure (including the electrodes) has particular requirements, as it needs to be transparent for some energies and absorbing for others. Current research on perovskite–silicon tandem solar cells solves some of these issues. Still, perovskite solar cells have challenges on their own, e.g., stability[5] and the incorporation of toxic materials.[6]

Organic photovoltaics is an emerging photovoltaic technology approaching commercial viability as demonstrated by single cell efficiencies around 20%[7] and small module efficiencies of up to 14.46%.[8] Recently, a "rainbow" tandem solar cell has been demonstrated, where two organic subcells were arranged laterally.[9] Lateral multi-junction architectures have the potential to be more cost-effective to produce than those stacked vertically, as they avoid the technological complexity of having to flawlessly deposit a multitude of layers.[9,10] Thus, they are likely to be more competitive in the solar cell market.[3] Furthermore, techniques such as digital printing[11,12] could allow such lateral multijunctions to be patterned with micrometer resolution.

Lateral tandems consist of two (or possibly more) subcells placed next to each other. However, because each subcell is optimized only for a particular portion of the solar spectrum, direct illumination by sunlight brings two key problems. First, the subcell with the higher energy bandgap does not convert the lower energy portion of the spectrum at all. Second, the aforementioned thermalization losses continue to be an issue for the subcell with the lower energy bandgap. As such, without a light management strategy, lateral tandem solar cells cannot directly use the total solar spectrum, resulting in a much lower power conversion efficiency than vertically stacked ones.

To mitigate this drawback, a solar spectral splitter can be placed above the solar cells. Such a photonic component enhances the power conversion efficiency by redirecting different spectral components of the sunlight to different single-junction cells according to their absorption spectrum.[13–17] Different mechanisms have previously been considered to solve this light management problem. One often employed mechanism is an arrangement of (semi-transparent) mirrors. This geometry exploits light trapping effects to split the solar spectrum in the desired manner. In addition, Ref. 18 demonstrates that light trapping with mirrors is theoretically allowed for any angle of incidence. However, the setup requires complicated photovoltaic fabrication considerations with respect to the geometrical arrangement. Another mechanism for spectral splitting is holographic lenses that make use of volume holographic elements with high diffraction efficiency to steer the flow of light.[14,19] For example, Ref. 20 demonstrates a 20% enhancement of energy yield over a single-bandgap device (at normal incidence) and moderate tolerance to a change in the angle of incidence ($\pm 11^\circ$ and $\pm 19^\circ$ tolerances in the in-device-plane and out-of-plane directions, respectively). Single-axis solar tracking is still required to achieve high power conversion efficiency in these systems.

Diffractive optical elements based on structured dielectric surfaces can also provide high diffraction efficiency and provide substantial design freedom for light management. Reference 20 designed a single-layer solar spectral splitter and measured 70% splitting efficiency at normal incidence. However, the performance of this device rapidly degraded away from normal incidence, dropping to half of its peak value at a $\pm 2^\circ$ in-plane incidence angle. Essentially, a single-layer device always redirects a given plane wave by approximately the same angle, irrespective of the incidence angle. Therefore, when moving away from normal incidence, the spectrally redirected light hits an adjacent subcell, which either cannot absorb that wavelength at all or suffers from increased thermalization losses. Such a misrouting quickly causes the observed degradation. In this contribution, we aim at designing a purely photonic device that enhances the power conversion efficiency of lateral tandem solar cells across a wider range of incidence angles. To achieve this, we inverse design a two-layer solar spectral splitter on top of a lateral tandem solar cell.

The parameters of the whole setup were chosen according to a theoretical study published recently.[3] The spectral splitter enables the device to enhance its performance over a wide range of angles. Conceptually, one can imagine that the first mask of the device redirects the incident light to a single-angle direction, for example, normal incidence. Next, the second mask spectrally distributes the light such that it can be harvested by the laterally arranged tandem solar cell. Notice that since we only optimize for the final functionality, the resulting device will not exactly incorporate this conceptual idea.

The inverse design process utilizes topology optimization[21–23] together with Fourier optics calculations and the thin element approximation, which enable us to optimize over many wavelengths and incident angles on a timescale of minutes. The figure of merit (FOM) maximized during optimization is the current density under prescribed illumination conditions. In essence, this is equivalent to maximizing the power conversion efficiency (for a fixed cell technology). To quantify the improvement due to the splitter, we define the relative current gain with respect to a single-junction solar cell comprising the best of the two tandem materials.

When optimizing a device to maximize its performance at normal incidence $\pm 1^\circ$, we achieve a relative current gain of 56.95% or more within this range. However, a device that merely performs at normal incidence $\pm 1^\circ$ is only useful when mounting the device on a motor-controlled stage to track the motion of the sun. Such a motorized system is expensive in acquisition and maintenance and therefore should be avoided. Instead, we focus on optimizing a device that performs over a wide range of incident angles. Although the maximum relative current gain is smaller, only 38.70%, a device optimized for an angle range of $\pm 20^\circ$ maintains a net gain over an angular range as large as $\pm 17^\circ$. In addition, we exploit the flexibility of our methodology to design devices that preferentially boost the performance at particular angles, which could correspond to times of the day when energy prices are generally higher.

II. RESULTS AND DISCUSSION

We aim to design a solar spectral splitter with high spectral splitting efficiency across a wide range of incident angles. When combined with lateral tandem solar cells, this will result in a device that provides a high power conversion efficiency over various relative positions of the sun. Figure 1 shows a schematic of our device and a conceptual overview of the design objective. The solar spectral splitter consists of two phase masks placed sequentially along the optical path, implemented by free-form structured surfaces at the top and bottom layers of a 200 μm long SiO_2 substrate. As we will see, having more than one phase-modulating surface is essential for achieving a wide-angle tolerance. Two tandem solar cells are placed directly underneath the spectral splitter at a distance of 2000 μm. The solar cells are 195 μm wide with a dead zone at each end of 2.5 μm, chosen according to a theoretical study.[3] The two subcells form a multi-junction architecture and are connected in series. Organic semiconductor materials encompass a broad range of optical bandgaps and energy levels. This provides us with a large

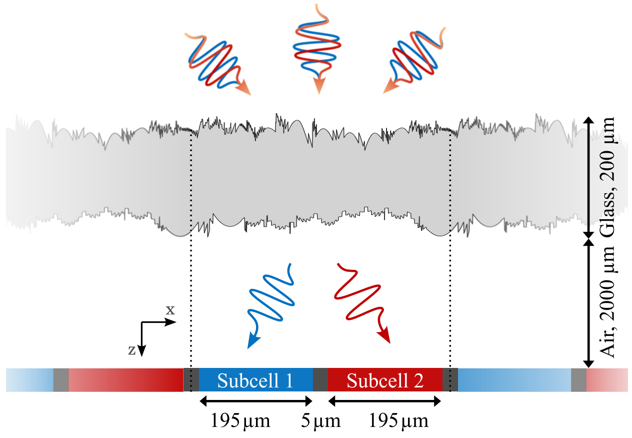

FIG. 1. Schematic of the considered setup with the inverse designed solar spectral splitter and the lateral solar cells. The blue subcell 1 absorbs at shorter wavelengths, and the red subcell 2 absorbs at longer wavelengths.

design freedom. Here, we assume an ideal case, where the solar cells convert wavelengths solely within their operational range, specifically 310–780 nm for the left (blue) subcell and 780–1340 nm for the right (red) device. We assume that the solar cells do not exhibit any back reflection. Given the definition of our objective function (see details in Sec. IV), the ideal splitter would redirect all the short wavelength components of the illumination to the left subcell and all the long wavelength components to the right subcell. This functionality should be provided, ideally, independent of the incident angle of the light. Note that the structure shown in Fig. 1 is one unit cell within a spatially periodic device. Finally, we emphasize that all these parameters are only exemplary. Although the quantitative results depend on these parameters, our design framework applies to any other related device.

In particular, for a given light spectrum, our goal is to maximize the average current generated by the tandem solar cells across the target angle range. The spectrum that we consider is the typical AM 1.5 spectrum of the sun,[2] weighted by a factor $\cos(\theta)$ to account for the total reduction in power due to the tilt θ of the device away from normal incidence. We sample this spectrum at $N_\lambda = 100$ equidistant wavelengths between 310 and 1340 nm. We initialize the incoming field for a given incidence angle as a sum of plane waves with amplitudes corresponding to the weighted AM 1.5 spectrum. We then simulate the propagation of this field through the system, using Fourier optics and the thin element approximation, and record the wavelength-dependent field intensity arriving at each subcell; see Sec. IV A. From this, we can calculate the current generated by the tandem solar cells by integrating the radiant flux over all wavelengths; see Sec. IV B. In the context of diffractive optical elements, the validity of Fourier optics and the thin element approximation was previously demonstrated by comparison to full-wave simulations.[24] To validate Fourier optics and the thin element approximation in our specific problem setup, we similarly used finite-element full-wave simulations, as shown in the supplementary material. Finally, we repeat this process for the N_θ angles and calculate the current averaged over the target angle range. This current constitutes our figure of merit, which we aim to maximize by using inverse design techniques to optimize the surface structures of the spectral splitter.

To enable efficient optimization, our code is developed using JAX,[25] a software library that automatically differentiates native Python and NumPy code. The differentiable formulation allows us to compute the derivatives of the simulation results with respect to the height profiles of the two phase masks.[21,22] By performing a single "backward" pass through the simulation code, we can obtain all derivatives simultaneously, maintaining computational complexity similar to that of the original function, regardless of the number of design variables used to parameterize the phase mask.[26–28] As such, we use a gradient descent algorithm to iteratively refine the phase masks to a design that maximizes the total current.

To motivate our research goal and emphasize the necessity of two phase masks, let us start by presenting results for a single phase mask and highlight the problems that arise when considering oblique angles of incidence. In particular, we optimize only the top layer of the spectral splitter while leaving the bottom layer as a flat interface, thus imparting no phase shift.

First, we design this structure to provide an optimal performance at normal incidence only, without considering its performance at any oblique angles. The resulting design is shown in Fig. 2(a). It mostly consists of blazed-grating-like sawtooth structures reminiscent of Fresnel lenses, with different periodicities on the left and right sides of the unit cell. The difference between the minimal and maximal height of the structure is 3.24 μm along the z axis. We call this quantity the maximum peak-to-valley height. Figure 2(e) shows the performance of this design when optimizing for 15 different incident angles equidistantly spread between -5° and 5°. To ensure that the optimization is not overly tailored to the optimized angles, the testing angles shown in the figure are deliberately chosen to differ. The angles of illumination are indicated by the different color schemes from yellow to red and from aqua to blue. The blue curves illustrate the transmitted light onto the left solar cell 1, while the red curves represent the light transmitted onto the right solar cell 2. An ideal device would correspond to a transmission plot for each subcell that looks like a step function, regardless of the incidence angle. For the left subcell (indicated by the blue background shading), this would correspond to 100% transmission for the short wavelengths and 0% transmission for the long wavelengths. We find that the optimized device performs very well at normal incidence (shown by the dark blue and red curves), in agreement with the results from Ref. 20. However, as we see in Fig. 2(e), there is a rapid degradation in the performance away from normal incidence. As we approach angles of $\pm 2.5^\circ$, we do not observe any splitting behavior any more. Indeed, the results further deteriorate for angles around $\pm 5^\circ$ (shown by the aqua and orange curves), where we see that the splitting is in fact totally inverted.

To combat this issue, we try to explicitly account for the device's performance away from normal incidence by encoding it into the objective function. In particular, we calculate the current generated for a range of different illumination angles and then consider our objective function as the average current across this range of angles. Such a device optimized for 50 angles in the range $\pm 5^\circ$ is shown in Fig. 2(b). The resulting device has a very rough, non-periodic profile with a maximum peak-to-valley height of 4.62 μm. Unfortunately, as we see in Fig. 2(f), this approach is unsuccessful for a

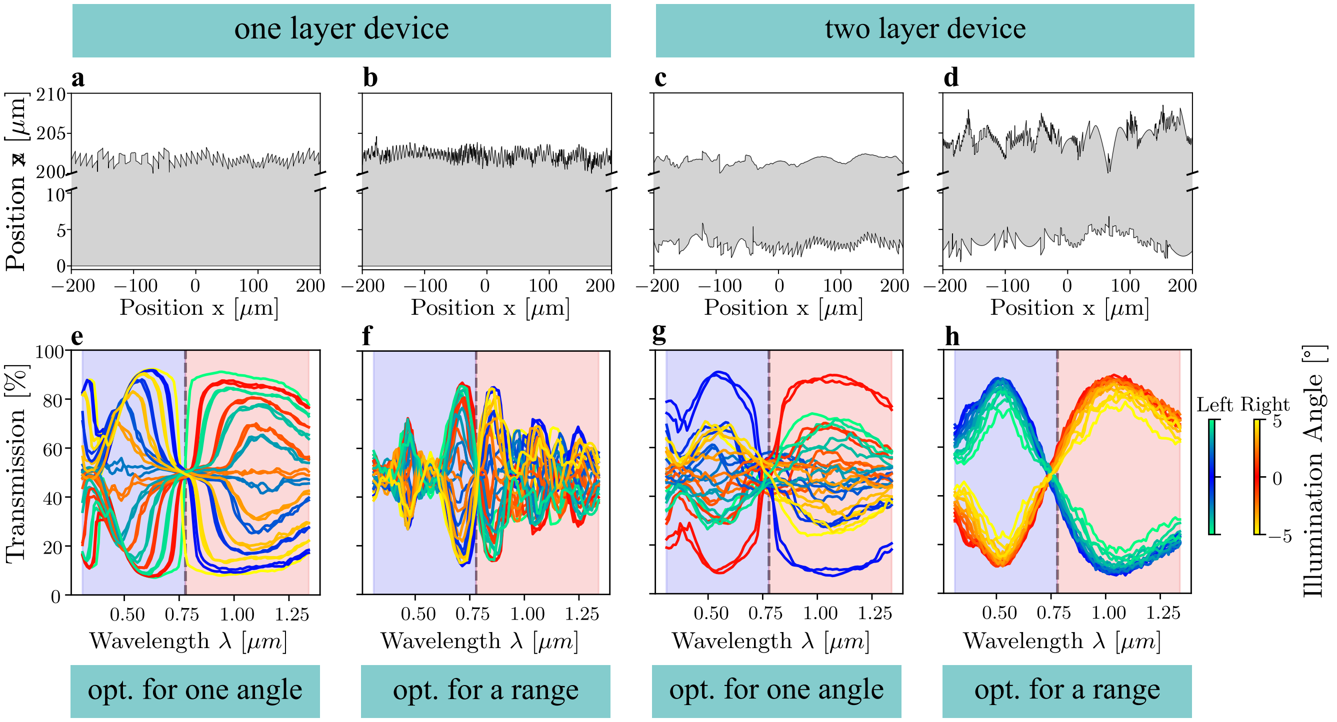

FIG. 2. Comparison of different devices. The top row shows the device layout. The corresponding maximum peak-to-valley height can be found in Table 1 of the supplementary material. The bottom row shows the performance. (a) One-sided phase mask optimized for 0° only. (b) One-sided phase mask optimized for 50 angles between −5° and 5°. (c) Two-sided phase mask optimized for 0° only. (d) Two-sided phase mask optimized for 50 angles between −5° and 5°. (e) Performance of the one-sided solar spectral splitter optimized at an angle of 0° only. (f) Performance of the one-sided solar spectral splitter optimized for angles between −5° and 5°. (g) Performance of the two-sided solar spectral splitter optimized at an angle of 0° only. (h) Performance of the two-sided solar spectral splitter optimized for angles between −5° and 5°. In [(e)–(h)], the transmission onto the left (blue and aqua curves) and right (red and orange curves) subcells is shown separately for a total of 15 incident fields illuminating the device at equidistant angles between −5° and 5°. These are not identical to the optimization angles.

single phase mask. The optimizer cannot find any suitable device and instead delivers a device that has an entirely random and unhelpful performance at any incidence angle in the range of ±5°. Indeed, we conjecture that it may be simply impossible to achieve the desired functionality with a single free-form-surface phase mask.

This realization motivates us to study two-layer phase masks in the rest of this article. To motivate the second key ingredient in our final design strategy, we present results for a two-layer phase mask optimized only for normal incidence. The design and results are shown in Figs. 2(c) and 2(g). The top layer design is much smoother than the bottom one. The maximum peak-to-valley height is 2.74 μm for the top and 4.73 μm for the bottom layer. At 0°, we observe a distinct splitting of the different wavelengths onto the different solar cells. It looks similar to an ideal boxcar result. However, the results quickly become much worse for larger illumination angles, at some point resulting in a (noisy) flat response, corresponding to a zero splitting efficiency. At even larger angles around ±5°, the transmission response is again inverted, but much less so compared to the single-layer design. In conclusion, even when only optimized for normal incidence, the two-layer device already performs better than the one-layer device, both in terms of its splitting efficiency at normal incidence and in terms of its angle insensitivity. Nonetheless, it is still not particularly robust toward different illumination angles. This is not surprising considering we did not optimize it to be so.

Therefore, in the same way as we attempted for a single phase mask, we can optimize a two-layer device that maximizes the current averaged over a range of angles. Again, we consider 50 angles in a range between ±5°. The design and results are shown in Figs. 2(d) and 2(h). The design exhibits similar roughness on both layers. The maximum peak-to-valley height is 8.47 μm for the upper and 6.23 μm for the lower layer. We observe the desired splitting of the different wavelengths onto the different subcells, with consistent behavior across the entire range of angles. The plot in Fig. 2(h) fulfills our expectation, with maximal transmission for the blue curve in the low wavelength range and maximal transmission for the red curve in the longer wavelengths. Naturally, the performance is better for those angles nearer the central optimization angle (normal incidence in this case). However, it is encouraging to note that a substantial increase in current over a device without a solar spectral splitter is maintained across the entire range of angles, as we will show below. Compared with the device optimized for one angle [Figs. 2(c) and 2(g)], this device optimized for a range of angles [Figs. 2(d) and 2(h)] has a less boxcar-like shape at normal incidence, corresponding to a smaller spectral splitting efficiency. However this performance is now consistently maintained across the entire angle range ±5°. We calculated the total amount of misdirected light that arrives at a subcell, which is not performant for that wavelength. This amount is ~20% for normal incidence, increasing up to approximately ~35% for 5°. Similar information can be directly read from Fig. 2. Namely, the red (blue) curve in the blue (red) region tells us the percentage of field intensity that arrives at the "wrong" subcell.

Having established and motivated our design strategy, we now investigate the robustness of this approach for even larger ranges of incidence angles. The idea is to show how our optimization potentially works for real-world applications in lateral tandem devices, where an enhanced performance is desired over wide angle ranges without the need for solar tracking.

Figure 3 shows the current density as a function of the angle of incidence for a few different devices optimized to perform over different ranges of angles, from narrow to wide. The dashed vertical lines indicate the width of the angular range considered in the optimization. The black line indicates a single-junction device made from the tandems' best performing material without light management. The dashed gray lines indicate the relative current gain (or loss) compared to the single-junction reference device. Notice that because we concentrate on demonstrating how our optical device improves a given lateral solar cell configuration, we do not compare our device to a vertically stacked tandem solar cell, and we do not introduce any optimizations for the single-junction device. We also note that as long as the operating voltage remains unchanged, current density is the appropriate metric for comparison.

Most devices achieve a relative current gain within their optimization ranges, but the gain quickly degrades outside this range. The trade-off between a peak performance for narrow optimization ranges vs a sustained performance across wider angles is clearly demonstrated in Fig. 3. For a small optimization range of ±1°, the current density at normal incidence is 50.10 A/m^2, which corresponds to a gain of around 57% compared to the single-junction device. Yet, this performance immediately decays for larger incidence angles. For larger optimization ranges, at normal incidence illumination, we only achieve a current density of 44.25 A/m^2, corresponding to a gain of 40% over the single-junction device. However, the decay of gain does not immediately occur. This means the more constrained the angular range considered in the optimization, the better the performance at the targeted angles. Similarly, the wider the angular range in the optimization, the less pronounced the peak performance, but the longer the performance is maintained. On the other hand, it is encouraging to note that when increasing the angular range from ±5° onward, the degradation of the peak performance is not well pronounced anymore, and it decreases only marginally. That being said, we see that for the largest possible angle range, it is not possible to see a positive relative current gain in the entire angular domain considered for the inverse design. This could be a hint that the constraints we impose in the optimization are too severe. A larger number of structured interfaces might mitigate the problem. However, this would come with a general device complexity that is undesirable. At the same time, due to the conservation of optical étendue, it is not possible to optimize the spectral splitter for the full, desired spectrum of ±90° for the setting given in this contribution.[29] For each wavelength separately, the splitter can be understood as a 2D solar concentrator achieving a concentration factor $C_{\max} = 2$ because each subcell occupies approximately half of the space available. The limit for the concentration factor is[30]

$$C_{\max} = \frac{\mathrm{NA}}{\sin\alpha}, \tag{1}$$

where NA is the numerical aperture of the device's optical elements and α is the maximum incidence angle. In our case, $C_{\max} = 2$ because each subcell fills half of the space. Thus, we find an angle limit $\alpha = \arcsin(\mathrm{NA}/2)$. If we conservatively estimate the numerical aperture of the splitter to be $\sin(\arctan[(\Lambda/2)/d]) \approx 0.1$, where Λ is the period and d is the splitter-to-subcell distance, we find $\alpha = 3°$ as the limiting angle. Our devices achieve gains less than 2 for angles ranging from 1° to 20°, so it is reasonable to assume that they perform close to or below the étendue limit.

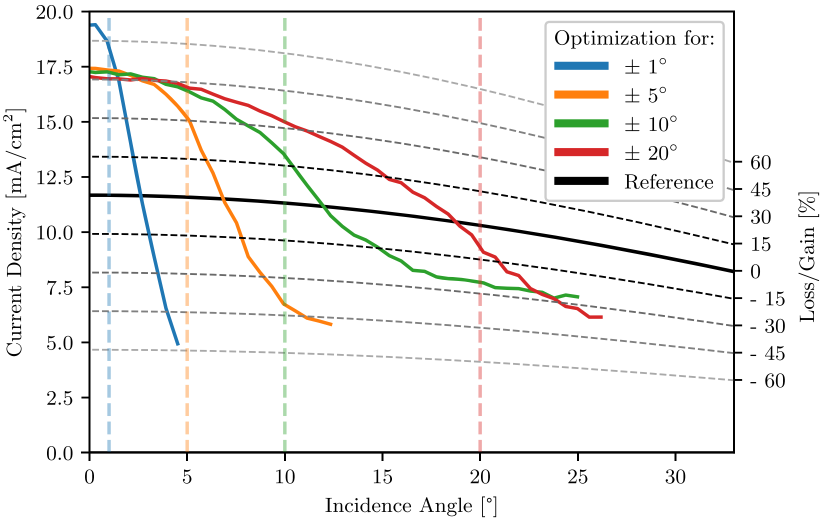

FIG. 3. Current density as a function of the angle of incidence for a set of devices optimized over different angle ranges. The dashed colored vertical lines indicate the target angle range (i.e., the range over which the device was optimized to perform). The black curve indicates a reference single-junction device made from the tandems' best performing material without light management. The dashed gray curves indicate the relative current gain (or loss) compared to the reference device (as indicated in the right-hand side vertical axis).

One can observe that the design in Fig. 2(d) combines features that look like diffractive lenses with faster-varying grating-like structures. In the 2D field profiles shown in supplementary material Sec. 6, we observe that the first interface seems to partially focus light onto several distinct regions of the second interface. These regions shift with the angle of incidence. At the same time, unambiguous spectral splitting occurs only after the second interface, in the region near the solar cells. It thus appears that each interface might be specialized toward either dealing with different incidence angles or performing the wavelength separation. This also suggests that it might be possible to replace one of the structured layers with an array of (cylindrical) microlenses, for example, if this would simplify fabrication. However, such an interpretation of our device is only approximate. The field profiles show that these two functionalities—spectral splitting and angular robustness—are partially shared between the two interfaces. Thus, it is not clear that enforcing a strict separation of tasks would provide an improvement. Comparing the performance of this device to one based on microlenses and only one free-form surface could be a topic of future studies.

Tight fabrication tolerances can pose challenges for production, resulting in reduced yield and increased overall cost. Robustness to dimensional inaccuracies are an important aspect for any photonic design. Therefore, we investigated the robustness of the splitting performance of our device, by running additional simulation studies with perturbed geometries and materials. The studies and their results can be found in Sec. 4 of the supplementary material. The performance was found to be sufficiently robust within variations that are achievable with modern fabrication technologies. All in all, the perturbation strength without any significant performance loss ranges from a few micrometers relative offset between the two phase masks to tens of micrometers for thickness variations of the glass block and hundreds of micrometers tolerance in the separation between phase masks and solar cells. In addition, moderate variations in refractive index and in stochastic noise of the masks' height profiles can be tolerated. Comparable fabrication tolerances were achieved for a similar phase mask that used a pre-compensation procedure from our previous publication.[31] Beyond fabrication related imperfections, surface damage may also arise from outdoor exposure. A straightforward strategy to mitigate such damage is the application of a protective layer with a low refractive index. If the layer is made from a hydrophobic material, it could even allow self-cleaning. Rainwater would remove accumulated dust, preserving optical performance over time.

To further highlight the possible use of wide-angle tolerant solar spectral splitters for real-world applications and the flexibility of our design method, we optimize devices that have a peak performance at an oblique angle of incidence. Depending on the orientation of the device, we might envisage that such angles are suitable for devices geared to maximize the power conversion in the morning or evening hours when the cost of energy is typically higher,[32] and an increase in current production could be especially beneficial. Furthermore, this could be useful for building integrated photovoltaics, where modules will not necessarily have normal incidence at peak sun illumination.

Figure 4 depicts the relative current gain for devices optimized over an angle range of ±10° centered at 0°, 10°, and 20° degrees. Note the gray shading starting at around ±20°, where the thin element approximation becomes less reliable; see Sec. IV A. Each device shows a relative current gain for its corresponding optimized angle range. Thus, our method works for ranges of incident angles that do not need to be centered around normal incidence. However, a slightly higher and broader gain can be noted for the optimization around normal incidence. This can be explained by the fact that more slanted angles are difficult for the setup to optimize since they need stronger rerouting by the solar spectral splitter.

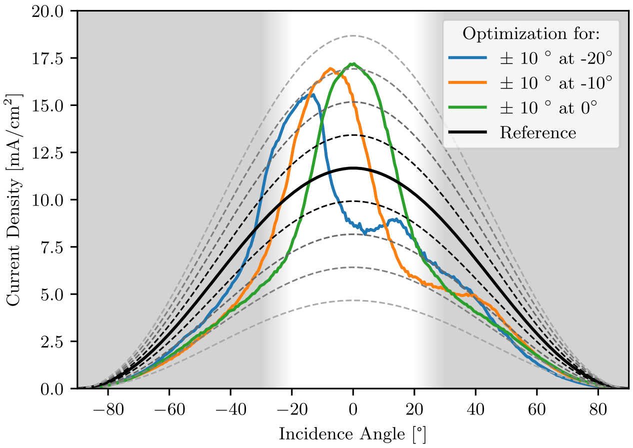

FIG. 4. Optimization of solar spectral splitters with target incidence angles ±10° centered around −20°, −10°, and normal incidence 0°. The gray color shading starting at ±20° toward larger angles shows the regime where the thin element approximation becomes increasingly less reliable. The reference for the relative current gain is a single-junction device made from the best performing material (subcell 1, left). It is indicated in black. The dashed gray curves show the relative current gain (or loss) compared to the reference device. The relative gain/loss is depicted in steps of 15% starting from the reference curve.

III. CONCLUSION

In conclusion, we used inverse design techniques to design wide-angle tolerant solar spectral splitters that enhance the power conversion efficiency over a large range of solar radiation incidence angles. In particular, we demonstrated a device that enhances the current-generation performance for around ±17°. We expect that this range can be pushed even further. However, we refrained from analyzing such cases, as the thin element approximation we utilized in our design method starts to become unreliable beyond ±20°. Depending on the requirements of any given device, one can tailor the width of the angle range over which an optimized device provides a performance enhancement. We showed that the difference in peak performance between, e.g., ±5° and ±20° was quite minimal, and thus, one can obtain good performance for even very wide angle ranges. Finally, we demonstrated the flexibility of our design method, with the ability to optimize devices that have a peak performance at oblique angles of incidence, perhaps corresponding to particular times of the day when the unit energy cost is highest. We highlighted that two phase masks are necessary for enabling the wide-angle tolerance of a solar spectral splitter for lateral tandem solar cells, combined with a design strategy that explicitly optimizes for a range of angles rather than just normal incidence.

Finally, it is important to note that our goal has been to improve the angular tolerance in the plane of the device (the x–z plane in Fig. 1), without considering how an out-of-plane (y–z plane) orientation impacts the performance. In Fig. S3 of the supplementary material, we show that a relative current gain is maintained for out-of-plane angles as large as ±50°. This implies that within the design constraints of a specific application, one would choose to orient our device to maximize coverage of the solid angle subtended by the sun's motion, ensuring that the device benefits from a relative current gain over the largest portion of this 2D angular range. The remaining variations in the solar trajectories throughout the year are due to earth's obliquity of its ecliptic, leading to variations of ±23.4° throughout the year. Therefore, the designed splitter having an in-plane angular tolerance of ±17° is an important breakthrough for light management in lateral tandems. For completeness, we note that there is no concentration of light in the out-of-plane direction. Thus, we do not expect optical étendue conservation to be a major limiting factor for the out-of-plane angle tolerance, unlike in the in-plane direction where it plays a large role.

IV. METHODS

A. Fourier optics and thin element approximation

Our solar spectral splitter is, essentially, a two-layered diffractive optical element. Powerful design methods exist to design structured interfaces that steer the incident light preferentially. These structured interfaces can be implemented either as a directly structured material layer[33] or, alternatively, as a metasurface.[34,35] Scalar diffraction methods such as Fourier optics have been successfully utilized in the field of metasurfaces for holography[36,37] and for the design of diffractive optical elements.[36,38,39] Fourier optics is a mathematical tool describing the propagation of light in the spatial frequency domain.[40]

Let us consider a monochromatic field $E_0(x,\lambda)$ that has the plane wave decomposition (obtained through the Fourier transform) $\tilde{E}_0(k_x,\lambda)$ with k_x the wavenumber and λ the wavelength. This field, along with the structures we consider, is invariant in the out-of-plane y-direction. The propagation of $\tilde{E}_0(k_x,\lambda)$ through a medium of refractive index n for a distance z is given by

$$\tilde{E}_1(k_x,\lambda) = \tilde{E}_0(k_x,\lambda)\exp\left(\mathrm{i}z\sqrt{\left(\frac{2\pi}{\lambda}n\right)^2 - k_x^2}\right). \tag{2}$$

The above equation allows us to propagate an optical field in a computationally inexpensive, one-step manner, which is essential due to the large distances compared to the wavelength involved in the solar spectral splitter. The theory is described further in Chap. 4 of *Fundamentals of Photonics.*[40]

When passing through a lens or an optical element, the incident field $E_0(x,\lambda)$ at position x with wavelength λ undergoes a phase shift. Within the thin element approximation, up to an unimportant global factor, this phase shift is given by

$$E_1(x,\lambda) = E_0(x,\lambda)\exp\left(\mathrm{i}\frac{2\pi}{\lambda}(n-1)d(x)\right), \tag{3}$$

where $d(x)$ is the thickness of the material with refractive index n (see Sec. 2.4 in Ref. 40 for details). The thin element approximation is valid when both the maximum thickness of the element d_0 and the angle of incidence of the light θ are sufficiently small such that $(d_0/\lambda)\theta^2/2n \ll 1$. With the parameters we use, our results are robust up to angles of ±20°. We furthermore ignored reflections at the material interfaces, but this is a fairly minor approximation because of the low refractive index of SiO_2 and the absence of very oblique angles of incidence. We verified the validity of these approximations by comparing them with full-wave simulations (see the supplementary material). Furthermore, the same approach was also previously used to design optical phase masks whose optical performance was verified by experiments.[31] The exact intensity distribution of the light in 2D was also visualized. For details, see Sec. 6 of the supplementary material.

B. Solar cell current

We aim to maximize the short circuit current $J_{\mathrm{sc,tot}}$ of the lateral tandem setup over all considered wavelengths. We influence this current by changing the E-field $E(x,\lambda)$ reaching the lateral subcells after passing through the spectral splitter. Therefore, we need to find the theoretical description linking $E(x,\lambda)$ to $J_{\mathrm{sc,tot}}$. In the following, we use a mathematical description, based on the explanations found in Part 2 of Ref. 2.

The input irradiance on the top layer of the solar spectral splitter is given by the typical AM 1.5 spectrum of the sun,[2] and we multiply it by a factor $\cos(\theta)$ to account for the reduction in power due to the tilt θ of the device. The considered setup through which the light propagates is shown in Fig. 1. As a reminder, the left lateral subcell 1 converts light in the range from 310 to 780 nm and the right lateral subcell 2 from 780 to 1340 nm. The black area between the two solar cells is the "dead zone," where no light is converted into current. To implement this in our code, we simply multiply the field by a boxcar function representing the region where absorption occurs.

If we consider one wavelength, a light intensity $|E(x,\lambda)|^2$ arrives on the ith solar cell. We then integrate this over the x and y dimensions of the solar cell. The integration along the y direction simply results in a constant factor as the device is invariant along this axis. As such, the radiant flux $\mathrm{P_i}(\lambda)$ for the ith solar cell is

$$\mathrm{P_i}(\lambda) = \frac{cn\varepsilon_0}{2}\iint_{x_{i,\mathrm{L}}}^{x_{i,\mathrm{R}}} |E(x,\lambda)|^2\, dx\, dy, \tag{4}$$

where $x_{i,\mathrm{L}}$ and $x_{i,\mathrm{R}}$ are the left and right boundaries of the ith subcell, n is the refractive index, which is modeled as 1.45 for SiO_2, and ε_0 is the vacuum permittivity. Next, we integrate $\mathrm{P_i}(\lambda)$ over all considered wavelengths, and we calculate the ith single-junction short circuit current as

$$J_{\mathrm{sc,i}} = \frac{e}{hc}\int \mathrm{EQE}(\lambda)\cdot\lambda\cdot\mathrm{P_i}(\lambda)\, d\lambda, \tag{5}$$

where $\mathrm{EQE}(\lambda)$ is the external quantum efficiency, e is the elementary charge, and h is the Planck constant. $\mathrm{EQE}(\lambda)$ values of up to 90% are typically reached for state of the art organic photovoltaic blends. We assume a wavelength-independent absorption of each subcell in their corresponding wavelength range. This means,

$$\mathrm{EQE}(\lambda) = \begin{cases} 0.9, & \lambda_{\min} \le \lambda \le \lambda_{\max} \\ 0, & \text{otherwise.} \end{cases} \tag{6}$$

Typically, lateral multi-junction solar cells are connected in series. Kirchhoff's current law thus enforces equal currents through both solar cells, resulting in a reverse bias to the subcell with higher $J_{\mathrm{sc,i}}$ when the tandem is short circuited, resulting in a reduced overall current (and reduced power conversion efficiency). As a first order approximation, this effect can be modeled as $J_{\mathrm{sc,tot}} = \min_i(J_{\mathrm{sc,i}})$. To avoid the discontinuous derivative of this model, we introduce a smooth minimum as

$$J_{\mathrm{sc,tot}} = J_{sc,1} + J_{sc,2} - \frac{1}{\alpha} \cdot \log\left(e^{\alpha \cdot J_{sc,1}} + e^{\alpha \cdot J_{sc,2}}\right), \tag{7}$$

where we set the positive parameter α equal to 40. This equation replicates the effect of a finite equivalent parallel conductance of the forward biased subcell (see the supplementary material for further details). With Eq. (7), we have obtained a differentiable expression for the short circuit current of the full tandem. This enables us to perform gradient based optimization to maximize $J_{\mathrm{sc,tot}}$.

C. Simulation and optimization

Topology optimization is an inverse design strategy used in the photonic community to find optical structures.[41,42] Given a specific desired figure of merit (FOM), the inverse design problem aims to maximize or minimize the FOM of the system while obeying imposed constraints. The solution of the inverse design problem leaves us with a locally optimal structure of the setup.[21,23] In particular, we calculate the optical fields with Fourier optics and the thin element approximation and then use gradient-based algorithms to iterate toward an optimized device. All the gradients are obtained with one forward and one backward (so-called "adjoint") pass through the simulation.[22]

Our simulation is written in Python. We use a one-dimensional simulation grid along the x axis, with a width of 400 μm and 1000 sampling points. We parameterize the surface topographies of the device in a free-form manner, with the same resolution as the simulation grid itself. Therefore, the $2N_x = 2000$ input parameters are the heights of the two surfaces at the discretized points along the x axis. We initialize the optimization cycle with two flat topographies, i.e., with surface heights of zero everywhere. The two solar cells have a width of 195 μm along the x axis and a dead zone of 5 μm in-between each cell. Notice that our simulation integrates periodic boundary conditions along the x axis, meaning that a small bandgap device lies between two large bandgap devices and vice versa. The thickness of the SiO_2 glass between the two optimized layers is set to 200 μm, and the distance of air between solar cells and the phase masks is 2000 μm. See the setup in Fig. 1. Our simulation code and gradient calculations allow us to optimize over 50 wavelengths and incident angles between ±20° on a timescale of minutes.

We seek an optimal phase mask profile through gradient-based local optimization. This means we want to maximize our desired figure of merit, namely, the total current of the setup given by Eq. (7), while respecting the imposed constraints of our problem, in this case, the bandgap requirements.[21,22] To optimize with any chosen optimizer, we need a method to calculate the gradients of the fields from our simulation concerning their design variables—in our case, the height profile of the phase mask. To accomplish this, we use the software package JAX,[25] which automatically obtains the derivatives of native Python and NumPy code with a straightforward interface.

We use the Adam optimizer as implemented in the Optax JAX package[43] for optimization. Adam is a variant of stochastic gradient descent (SGD) that leverages momentum and adaptive learning rates for each parameter, which often outperforms naive SGD in practice.[44] For our optimization, we set the learning rate α_t to 0.1 and kept the other parameters as given in the standard settings of the optimizer, such as $\beta_1 = 0.9$ and $\beta_2 = 0.999$.

SUPPLEMENTARY MATERIAL

The supplementary material provides detailed peak-to-valley height data, validates our method with full-wave simulations, and analyzes the out-of-plane angular tolerance and robustness of the device. It also elaborates on current matching in our setup and shows 2D intensity distributions.

ACKNOWLEDGMENTS

The airmass irradiance dataset was obtained from the U.S. Department of Energy (DOE)/NREL/AL-LIANCE. M.L.S. and J.D.F. acknowledge the Karlsruhe School of Optics and Photonics (KSOP). Part of this work has been supported by the Helmholtz Association in the framework of the innovation platform "Solar TAP." T.J.S. acknowledges funding from the Alexander von Humboldt Foundation. M.N. and C.R. acknowledge support by the Karlsruhe Institute of Technology through the "Virtual Materials Design" (VIRTMAT) project. C.J.B. and L.L. acknowledge financial support from the DFG (Grant Nos. BR 4031/22-1 and BR 4031/21-1).

AUTHOR DECLARATIONS

Conflict of Interest

The authors have no conflicts to disclose.

Author Contributions

M. L. Schubert: Conceptualization (equal); Data curation (equal); Investigation (equal); Methodology (equal); Software (equal); Validation (equal); Writing – original draft (equal). **J. D. Fischbach**: Conceptualization (equal); Data curation (equal); Investigation (equal); Methodology (equal); Software (equal); Writing – original draft (supporting). **M. Nyman**: Conceptualization (equal); Methodology (equal); Software (supporting); Validation (equal); Writing – original draft (supporting). **L. Lüer**: Conceptualization (equal); Investigation (supporting); Writing – original draft (supporting). **C. J. Brabec**: Conceptualization (supporting). **C. Rockstuhl**: Conceptualization (equal); Supervision (lead); Writing – original draft (supporting). **T. J. Sturges**: Conceptualization (equal); Data curation (equal); Investigation (equal); Methodology (equal); Supervision (equal); Writing – original draft (equal).

DATA AVAILABILITY

The data that support the findings of this study are available from the corresponding author upon reasonable request.

REFERENCES

[1] A. Richter, M. Hermle, and S. W. Glunz, "Reassessment of the limiting efficiency for crystalline silicon solar cells," IEEE J. Photovoltaics **3**, 1184–1191 (2013).

[2] A. Smets, K. Jäger, O. Isabella, R. van Swaaij, and M. Zeman, *Solar Energy—The Physics and Engineering of Photovoltaic Conversion, Technologies and Systems* (UIT Cambridge, Ltd., England, 2016).

[3] L. Lüer, I. M. Peters, V. M. L. Corre, K. Forberich, D. M. Guldi, and C. J. Brabec, "Bypassing the single junction limit with advanced photovoltaic architectures," Adv. Mater. **36**, 2308578 (2024).

[4] F. I. for Solar Energy Systems ISE, Press release: Fraunhofer ise develops the world's most efficient solar cell with 47.6 percent efficiency, 2022, https://www.ise.fraunhofer.de/en/press-media/press-releases/2022/fraunhofer-ise-develops-the-worlds-most-efficient-solar-cell-with-47-comma-6-percent-efficiency.html.

[5] T. A. Chowdhury, M. A. Bin Zafar, M. Sajjad-Ul Islam, M. Shahinuzzaman, M. A. Islam, and M. U. Khandaker, "Stability of perovskite solar cells: Issues and prospects," RSC Adv. **13**, 1787–1810 (2023).

[6] J. Li, H.-L. Cao, W.-B. Jiao, Q. Wang, M. Wei, I. Cantone, J. Lü, and A. Abate, "Biological impact of lead from halide perovskites reveals the risk of introducing a safe threshold," Nat. Commun. **11**, 310 (2020).

[7] S. Guan, Y. Li, C. Xu, N. Yin, C. Xu, C. Wang, M. Wang, Y. Xu, Q. Chen, D. Wang, L. Zuo, and H. Chen, "Self-assembled interlayer enables high-performance organic photovoltaics with power conversion efficiency exceeding 20%," Adv. Mater. **36**, 2400342 (2024).

[8] F.-A.-U. E.-N. (FAU), The most efficient organic solar module in the world comes from FAU and hi ERN, 2023, https://www.fau.eu/2023/12/19/news/research/world-record-in-solar-energy/.

[9] M. Gibert-Roca, M. Casademont-Viñas, Q. Liu, K. Vandewal, A. R. Goñi, and M. Campoy-Quiles, "Rainbow organic solar cells: Implementing spectral splitting in lateral multi-junction architectures," Adv. Mater. **36**, 2212226 (2024).

[10] J. Palassery Ithikkal, S. Izawa, and M. Hiramoto, "Doped lateral organic photovoltaic cells," Physica Status Solidi A **220**, 2300108 (2023).

[11] M. K. Hamjah, M. Steinberger, K. C. Tam, H. J. Egelhaaf, C. Brabec, and J. Franke, "Aerosol jet printed AgNW electrode and PEDOT: PSS layers for organic light-emitting diode devices fabrication," in *2021 14th International Congress: Molded Interconnect Devices, MID 2021—Proceedings* (Institute of Electrical and Electronics Engineers, Inc., 2021), pp. 1–4.

[12] R. Basu, K. S. Siah, A. Distler, F. Häußler, J. Franke, C. J. Brabec, and H.-J. Egelhaaf, "Aerosol-jet-printed encapsulation of organic photovoltaics," Adv. Eng. Mater. **25**, 2300322 (2023).

[13] B. Mitchell, G. Peharz, G. Siefer, M. Peters, T. Gandy, J. C. Goldschmidt, J. Benick, S. W. Glunz, A. W. Bett, and F. Dimroth, "Four-junction spectral beam-splitting photovoltaic receiver with high optical efficiency," Prog. Photovoltaics: Res. Appl. **19**, 61–72 (2011).

[14] B. D. Chrysler and R. K. Kostuk, "High energy yield bifacial spectrum-splitting photovoltaic system," Appl. Opt. **59**, G8–G18 (2020).

[15] A. Goetzberger, J. Goldschmidt, M. Peters, and P. Löper, "Light trapping, a new approach to spectrum splitting," Sol. Energy Mater. Sol. Cells **92**, 1570–1578 (2008).

[16] M. A. Green and A. Ho-Baillie, "Forty three per cent composite split-spectrum concentrator solar cell efficiency," Prog. Photovoltaics: Res. Appl. **18**, 42–47 (2010).

[17] L. Fan, M. Faryad, G. D. Barber, T. E. Mallouk, P. B. Monk, and A. Lakhtakia, "Optimization of a spectrum splitter using differential evolution algorithm for solar cell applications," Proc. SPIE **9191**, 91910I (2014).

[18] J. C. Goldschmidt, C. Do, M. Peters, and A. Goetzberger, "Spectral splitting module geometry that utilizes light trapping," Sol. Energy Mater. Sol. Cells **108**, 57–64 (2013), a part of Special Issue: Selected publications from the 22nd Space Photovoltaic Research and Technology (SPRAT) Conference.

[19] S. D. Vorndran, B. Chrysler, B. Wheelwright, R. Angel, Z. Holman, and R. Kostuk, "Off-axis holographic lens spectrum-splitting photovoltaic system for direct and diffuse solar energy conversion," Appl. Opt. **55**, 7522–7529 (2016).

[20] T. P. Xiao, O. S. Cifci, S. Bhargava, H. Chen, T. Gissibl, W. Zhou, H. Giessen, K. C. Toussaint, Jr, E. Yablonovitch, and P. V. Braun, "Diffractive spectral-splitting optical element designed by adjoint-based electromagnetic optimization and fabricated by femtosecond 3D direct laser writing," ACS Photonics **3**, 886–894 (2016).

[21] R. E. Christiansen and O. Sigmund, "Inverse design in photonics by topology optimization: Tutorial," J. Opt. Soc. Am. B **38**, 496–509 (2021).

[22] T. W. Hughes, M. Minkov, I. A. D. Williamson, and S. Fan, "Adjoint method and inverse design for nonlinear nanophotonic devices," ACS Photonics **5**, 4781–4787 (2018).

[23] P. R. Wiecha, A. Arbouet, C. Girard, and O. L. Muskens, "Deep learning in nano-photonics: Inverse design and beyond," Photonics Res. **9**, B182–B200 (2021).

[24] S. Mellin and G. Nordin, "Limits of scalar diffraction theory and an iterative angular spectrum algorithm for finite aperture diffractive optical element design," Opt. Express **8**, 705–722 (2001).

[25] Dataset: J. Bradbury, R. Frostig, P. Hawkins, M. J. Johnson, C. Leary, D. Maclaurin, G. Necula, A. Paszke, J. VanderPlas, S. Wanderman-Milne, and Q. Zhang (2018). "JAX: Composable transformations of Python+NumPy programs," Github. http://github.com/jax-ml/jax.

[26] A. Griewank and A. Walther, *Evaluating Derivatives: Principles and Techniques of Algorithmic Differentiation*, 2nd ed. (SIAM, 2008).

[27] A. G. Baydin, B. A. Pearlmutter, A. A. Radul, and J. M. Siskind, "Automatic differentiation in machine learning: A survey," J. Mach. Learn. Res. **18**, 5595 (2018).

[28] P. R. Wiecha, N. J. Dinsdale, and O. L. Muskens, "Deep learning driven data processing, modeling, and inverse design for nanophotonics," in *Integrated Nanophotonics* (John Wiley & Sons, Ltd., 2023), Chap. 7, pp. 245–275 https://onlinelibrary.wiley.com/doi/pdf/10.1002/9783527833030.ch7.

[29] M. Peters, J. C. Goldschmidt, and B. Bläsi, "Angular confinement and concentration in photovoltaic converters," Sol. Energy Mater. Sol. Cells **94**, 1393–1398 (2010), a part of Special Issue: National Conference on the Emerging Trends in the Photovoltaic Energy and Utilization.

[30] G. Smestad, H. Ries, R. Winston, and E. Yablonovitch, "The thermodynamic limits of light concentrators," Solar Energy Mater. **21**, 99–111 (1990).

[31] T. J. Sturges, M. Nyman, S. Kalt, K. Pälsi, P. Hilden, M. Wegener, C. Rockstuhl, and A. Shevchenko, "Inverse-designed 3D laser nanoprinted phase masks to extend the depth of field of imaging systems," ACS Photonics **11**, 3765–3773 (2024).

[32] E. SPOT, Market data, https://www.epexspot.com/en/market-data?market_area=DE-LU&trading_date=2024-06-06&delivery_date=2024-06-07&underlying_year=&modality=Auction&sub_modality=DayAhead&technology=&product=60&data_mode=table&period=&production_period=, 2024.

[33] S. N. Khonina, N. L. Kazanskiy, and M. A. Butt, "Exploring diffractive optical elements and their potential in free space optics and imaging- a comprehensive review," Laser Photonics Rev. **18**, 2400377 (2024).

[34] N. Yu, P. Genevet, M. A. Kats, F. Aieta, J.-P. Tetienne, F. Capasso, and Z. Gaburro, "Light propagation with phase discontinuities: Generalized laws of reflection and refraction," Science **334**, 333–337 (2011).

[35] M. Khorasaninejad, W. T. Chen, R. C. Devlin, J. Oh, A. Y. Zhu, and F. Capasso, "Metalenses at visible wavelengths: Diffraction-limited focusing and subwavelength resolution imaging," Science **352**, 1190–1194 (2016).

[36] A. C. Overvig, S. Shrestha, S. C. Malek, M. Lu, A. Stein, C. Zheng, and N. Yu, "Dielectric metasurfaces for complete and independent control of the optical amplitude and phase," Light: Sci. Appl. **8**, 92 (2019).

[37] G. Zheng, H. Mühlenbernd, M. Kenney, G. Li, T. Zentgraf, and S. Zhang, "Metasurface holograms reaching 80% efficiency," Nat. Nanotechnol. **10**, 308–312 (2015).

[38] D. C. O'Shea, T. J. Suleski, A. D. Kathman, and D. W. Prather, *Diffractive Optics: Design, Fabrication, and Test* (SPIE, 2004).

[39] M. E. Mustafa, M. Eich, and A. Y. Petrov, "Reciprocally tailored transparent artificial media for frequency and direction dependent light trapping," Opt. Mater. Express **14**, 1281–1292 (2024).

[40] B. E. A. Saleh and M. C. Teich, *Fundamentals of Photonics* (John Wiley & Sons, Inc., Hoboken, NJ, 2007).

[41] M. M. R. Elsawy, S. Lanteri, R. Duvigneau, J. A. Fan, and P. Genevet, "Numerical optimization methods for metasurfaces," Laser Photonics Rev. **14**, 1900445 (2020).

[42] P. R. Wiecha, A. Y. Petrov, P. Genevet, and A. Bogdanov, "Inverse design of nanophotonics devices and materials," Photonics Nanostruct.-Fund. Appl. **52**, 101084 (2022).

[43] I. Babuschkin, K. Baumli, A. Bell, S. Bhupatiraju, J. Bruce, P. Buchlovsky, D. Budden, T. Cai, A. Clark, I. Danihelka, A. Dedieu, C. Fantacci, J. Godwin, C. Jones, R. Hemsley, T. Hennigan, M. Hessel, S. Hou, S. Kapturowski, T. Keck, I. Kemaev, M. King, M. Kunesch, L. Martens, H. Merzic, V. Mikulik, T. Norman, G. Papamakarios, J. Quan, R. Ring, F. Ruiz, A. Sanchez, L. Sartran, R. Schneider, E. Sezener, S. Spencer, S. Srinivasan, M. Stanojević, W. Stokowiec, L. Wang, G. Zhou, and F. Viola (2020). "The DeepMind JAX ecosystem," Github. http://github.com/google-deepmind.

[44] D. Kingma and J. Ba, "Adam: A method for stochastic optimization," in International Conference on Learning Representations, 2014.